Accepted Manuscript

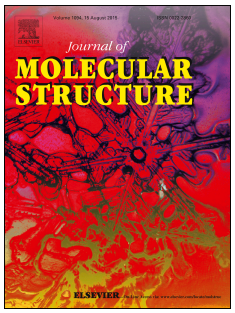

Synthesis, conformational analysis and molecular docking studies on three novel dihydropyrimidine derivatives

Lóide.O. Sallum, Wesley.F. Vaz, Nádia.M. Borges, Carlos.E.M. de Campos, Adailton.J. Bortoluzzi, Chris.H.J. Franco, Luciana.M. Ramos, Hamilton.B. Napolitano

PII: S0022-2860(19)30509-5

DOI: https://doi.org/10.1016/j.molstruc.2019.04.100

Reference: MOLSTR 26472

To appear in: *Journal of Molecular Structure*

Received Date: 7 December 2018

Accepted Date: 24 April 2019

Please cite this article as: Ló.O. Sallum, W.F. Vaz, Ná.M. Borges, C.E.M. de Campos, A.J. Bortoluzzi, C.H.J. Franco, L.M. Ramos, H.B. Napolitano, Synthesis, conformational analysis and molecular docking studies on three novel dihydropyrimidine derivatives, *Journal of Molecular Structure* (2019), doi: https://doi.org/10.1016/j.molstruc.2019.04.100.

Synthesis, conformational analysis and molecular docking studies on three novel dihydropyrimidine derivatives

Lóide O. Sallum[a], Wesley F. Vaz[a], Nádia M. Borges[a], Carlos E. M. de Campos[b], Adailton J. Bortoluzzi[b], Chris H. J. Franco[c], Luciana M. Ramos[a] and Hamilton B. Napolitano[a]*

[a]Universidade Estadual de Goiás, Anápolis, GO, Brazil

[b]Universidade Federal de Santa Catarina, Florianópolis, SC, Brazil

[c]Universidade Federal de Juiz de Fora, MG, Brazil

Abstract

The dihydropyrimidine (DHPM) derivatives **I**, **II** and **III** were synthesized through Biginelli reaction and characterized by X-ray diffraction and vibrational spectroscopic analyses (Raman and FTIR), whereas a conformational study was conducted. The results show that the DHPM **I**, **II** and **III** belong to the triclinic and monoclinic systems. In a general way, the crystal structure of these compounds are stabilized with N–H···O, O–H···O and N–H···S interactions. The C–H···π and π···π contacts were evaluated using the Hirshfeld surfaces. To evaluate eletronic properties of the DHPM set, theoretical calculations, using B3LYP/6-31G(d,p) method were undertaken. Also, the calculated infrared spectra with some global reactivity descriptors, the molecular electrostatic potential maps and frontier molecular orbital energies were obtained for these compounds. Finally, molecular docking was used to investigate the applicability of DHPM set as a tumor suppressor (L3MBTL1).

Keywords: *dihydropyrimidine; X-ray diffraction; molecular docking.*

Introduction

Heterocyclic chemistry is important in modern organic chemistry research [1]. The Biginelli [2] reaction represents a classical approach for the preparation of 3,4-dihidropyrimidin-2(1H)-ones by the one-pot condensation of an aromatic aldehyde, β-dicarbonyl and urea/thiourea in the presence of a mineral acid catalyst [3], basic catalyst [4], SiO_2-$CuCl_2$ [5], p-toluenesulfonic acid [6], Keggin and Dawson-type polyoxometalates [7], β-Cyclodextrin-propyl sulfonic acid [8] and others [9]. Numerous multifunctionalized dihydropyrimidine derivatives were obtained through cyclocondensation process, which increased their production considerably by using different substituents on all three building blocks. For this specific heterocyclic frame the acronym DHPM was adopted from the literature [3]. Heterocyclic DHPM have great importance in human biological system, once they are an essential part of natural products, various pharmacologically active molecules and nucleic acids. DNA & RNA base pairs (guanine, thymine, cytosine and adenine) are constituted by heterocyclic DHPM such as purine, pyrimidine and others. These heterocyclic DHPM can also be found in numerous drug candidates [9]. Although discovering a DHPM compound is an arduous and time-consuming process their applications to medicinal chemistry and its related fields are broad [10]. Some of the therapeutic and pharmacological properties of these DHPM are: antiviral, anti-inflammatory, anticarcinogenic, antibacterial, antihypertensive, calcium channel modulators, additionally, DHPM has promising application in the early suppression of breast cancer cells [11–15].

Thus, a comparative structural and supramolecular arrangement study is proposed involving 5-acetyl-3,4-dihydro-4-(4-hydroxy-3-methoxyphenyl)-6-methyl-2(1*H*)-pyrimidinone (DHPM **I**), the Ethyl-4-(4-hydroxy-3-methoxyphenyl)-6-methyl-2-thioxo-1,2,3,4-tetrahydropyrimidine-5-carboxylate (DHPM **II**) and 1-[1,2,3,4-tetrahydro-4-(4-hydroxy-3-methoxyphenyl)-6-methyl-2-thioxo-5-pyrimidinyl]-ethanone (DHPM **III**). The geometry optimization, global reactivity descriptors, molecular electrostatically potential and vibrational wavenumbers assignments for DHPM **I**, **II** and **III** were calculated at the B3LYP/6-31G (d,p) level of theory. In addition,

molecular docking analysis were made for these three compounds because of the biological activity of DHPM **I** against human Lethal (3) malignant brain tumor-like protein 1, L3MBTL1.

Experimental and computational procedures

Synthesis and crystallization

DHPM **I** was synthesized by the one-pot reaction of acetylacetone (0.300g, 3.00 mmol), 4-hydroxy-3-methoxybenzaldehyde (1.37 g, 9.00 mmol) and urea (0.18g, 3.00 mmol), whereas, to obtain DHPM **II,** ethyl acetoacetate (0.39g, 3.00 mmol), 4-hydroxy-3-methoxybenzaldehyde (1.37 g, 9.00 mmol) and thiourea (0.22g, 3.00 mmol) were used. Finally, acetylacetone (0.300g, 3.00 mmol), 4-hydroxy-3-methoxybenzaldehyde (1.37 g, 9.00 mmol) and thiourea (0.22g, 3.00 mmol), in the presence of MAI.Fe_2Cl_7 (5mol%) and 1 mL of BMI.BF_4 at 80ºC for 2 h, were used as a model reaction [17] to obtain DHPM **III**, as shown in scheme 1.

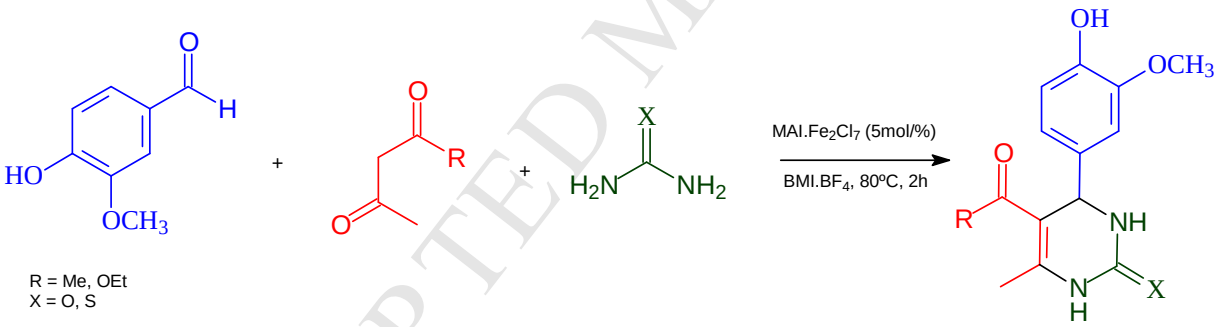

Scheme 1. Chemical scheme of the **s**ynthesized DHPM: [DHPM **I**] R = Me, X = O; [DHPM **II**] R = OEt, X = S and [DHPM **III**] R = Me, X = S.

The pure DHPM were obtained by filtering, drying and recrystallizing the precipitate with ethanol. Melting point measurements (Table S1) and infrared spectroscopic were used to analyze the purity of some samples. Infrared spectra were recorded on a PerkinElmer Frontier in the range 4000-400 cm^{-1} using the KBr pellet technique. DHPM **I**: White powder, m.p. 240 °C; FT-IR (KBr, cm^{-1}): 3343, 3298, 1691, 1638, 1527, 1442, 1377, 1331, 1240, 1037, 756. DHPM **II**: White powder, m.p. 220-222 °C; FT-IR (KBr, cm^{-1}): 3416, 3181, 2998, 1685, 1587, 1522, 1483, 1378, 1180, 1025,

751. DHPM **III**: Yellow powder, m.p. 238-239 °C; FT-IR (KBr, cm^{-1}): 3468, 3189, 2996, 1629, 1587, 1504, 1456, 1373, 1193, 1125, 752.

Crystals of DHPM **I**, **II** and **III** were grown from ethanolic solutions by slow evaporation method. Prismatic colorless crystals were obtained in a period of 15 days at room temperature (25ºC) with a semi-open bottle. To conduct the X-ray data collection, an appropriate single crystal was selected from homogeneous crystalline samples of each DHPM compound.

Crystallographic characterization

A single crystal for DHPM **I** and **III** were selected and data were collected on a Rigaku SuperNova diffractometer with AtlasS2 detector, using radiation MoKα (λ=0.71073 Å) at 293K. A single crystal for DHPM **II** was selected and a Bruker APEX 2 diffractometer was utilized to collect data, using CuKα (λ=1.54178 Å) at 110K. Direct methods were applied to solve these structures and least square methods to refine them using SHELX [18] in WingGX package [19]. The ellipsoids diagrams were generated from ORTEP [19] (Figure 1) and the packing diagrams were generating using Mercury [20]. Geometrical calculations were done using PLATON [21]. The non-hydrogen atoms were refined anisotropically. The Hydrogen bonded to Carbon and Nitrogen were placed geometrically and refined using a riding model with distance of N – H = 0.86 Å and aromatic C – H = 0.93 Å with Uiso(H) = 1.2 Ueq and 1.5 Ueq, respectively. The Crystallographic Information Files (CIF) of for DHPM **I**, DHPM **II** and DHPM **III** were deposited in the Cambridge Structural Data Base under codes 1882886, 1882887 and 1883842, respectively. Copies of the data can be obtained free of charge via www.ccdc.cam.ac.uk.

Hirshfeld surface

The Hirshfeld surface (HS) consists of a spatial map which makes use of color coding for representing the proximity of close contacts present around a certain molecule within a given network [22]. Two models of electron density are the means of obtaining the HS; such models

combine the overlapping of isolated molecules. These being illustrated by isolated spherical atoms, together with another one of interacting molecules, where $\boldsymbol{w_a(r)}$ is determined a weight function for each of the atoms in a molecule, as shown in Equation 1,

$$\boldsymbol{w_a(r) = p_a^{at}(r) / \sum_{i \in molecule} p_i^{at}(r)} \quad \text{(Eq. 1)}$$

where $\boldsymbol{p_i^{at}(r)}$ represents the electrical densities of the various spherically averaged atoms, whereas Equation 2 defines the electron density of an atomic fragment,

$$\boldsymbol{p_a(r) = w_a(r) p^{mol}(r)} \quad \text{(Eq. 2)}$$

$\boldsymbol{p^{mol}(r)}$ designates the molecular electron density. The normalized contact distance $\boldsymbol{d_{norm}}$ could be defined as the sum of the symmetric distances to the nearest atoms outside, ($\boldsymbol{d_e}$), and inside, ($\boldsymbol{d_i}$) of the surface. See Equation 3:

$$\boldsymbol{d_{norm} = (d_i - r_i^{vdw}) / r_i^{vdw} + (d_e - r_e^{vdw}) / r_e^{vdw}} \quad \text{(Eq. 3)}$$

$\boldsymbol{r_i^{vdw}}$and $\boldsymbol{r_e^{vdw}}$ are the atoms' van der Waals radii. Crystal Explorer 3.1 [23] was used to generate HS intermolecular interactions and the 2D fingerprint plots.

Powder Diffraction and Raman

X-ray powder diffraction for DPHM **I** and **II** were performed on an Advance DaVinci D8 diffractometer using CuKα (1.54056 Å) with Bragg-Brentano θ-θ geometry and LynxEye linear detector. The experimental data were collected in the 2θ range from 5° to 60°, in steps of 0.01° and accumulation time ranging from 0.5s to 1s by steps. X-ray powder diffraction for DPHM **II** was collected on a Xpert MPD diffractometer using CuKα (1.5418 Å) with Bragg-Brentano θ-θ geometry and Xcelerator linear detector. The experimental data were collected in the 2θ range from 5° to 55°, in steps of 0.0167° and 3 scans with accumulation time of 19.685 s by step. Fourier-

transform Raman spectroscopy for DPHM **I** and **II** were carry out using a Bruker RFS 100 spectrometer with Nd^{3+}/YAG laser operating at 1064 nm excitation line (near infrared region) and CCD detector with spectral resolution of 4 cm^{-1}. A good signal was obtained with 1024 scans. Raman spectra of different regions of a DHPM **II** sample surface were collected with 20x objective lens at room temperature using a PeakSeeker 785 (RAM–PRO–785) Raman system with a diode laser of 785 nm and 100 mW at the source. The backscattered Raman radiation was dispersed with a grating and focused on a Peltier-cooled charge-coupled device CCD detector allowing us to obtaining a spectral resolution of 6 cm^{-1}. All spectra were recorded at room temperature in the spectral window of (from 200 to 2000) cm^{-1} with same acquisition time (10 s).

Theoretical calculation

The theoretical calculations were made using the geometric parametres derived from the CIF files of each structure. These structures were optimized by means of Density functional theory (DFT) using the hybrid functional B3LYP and 6-31G(d,p) basis set with the Gaussian 09 package [24]. The absence of imaginary frequencies confirm that were obtained strucutures in a minima of energy, and so, it were used in the vibrational wavenumber calculations. The absence of imaginary frequencies confirm that geometries are in a minima of energy, and so, can be used in the vibrational calculations. The wavenumbers calculated were properly scaled [25] by the scale factor: 0.9620 and to assign the vibrational modes, the potential energy distribution analysis (PED) using VEDA4 program [26] was used in combination with the normal mode animations in GaussView. The same level of theory was used to calculate some global reactivity descriptors and to generate the frontier molecular orbitals (FMO) and molecular electrostatic potential map (MEP) .

Molecular docking

Molecular docking is the most widely used tool for exploring the interactions between an inhibitor molecule and the target protein. In our studies, the AutoDock-Vina software [27] was used

to carry this out. The crystallographic structure was downloaded from the Protein Data Bank, PDB (www.rcsb.org) [28]. Before docking, preparation of the ligand and receptor in Dock Prep [29] tool was necessary. Amid the protein preparation procedure, all missing hydrogen atoms were included, all water molecules and ligand erased, and the energy minimized utilizing Minimize Structure of Chimera. Protein and ligand were managed through the general AMBER force field 12SB [30]. The DHPM **I**, **II** and **III** were flexibly docked into the active site of the enzyme centered at the geometric point (16.67 Å x 40.11 Å x 32.92 Å) and grid size of 17 $Å^3$. Each and every other setting were kept as default setting.

Results and discussion

Solid State characterization

The ORTEP diagrams of DHPM **I**, **II** and **III** with their asymmetric units can be seen in Figure 1. These molecules exist in the screw boat conformation with C4 and N1 forming the flagpole atoms as described by Nayak et al. [31]. The carbonyl group C5=O2 appears in an s-cis conformation with respect to the C2=C3 double bond [32]. Arbitrarily S configuration was chosen for supramolecular analysis. The orientation of the methoxy group in the *meta* position is different in these forms, for DHPM **I** methoxy group bounded in ring inverted *meta* position (C10), although DHPM **II** and **III** bonded in ring standard *meta* position (C6).

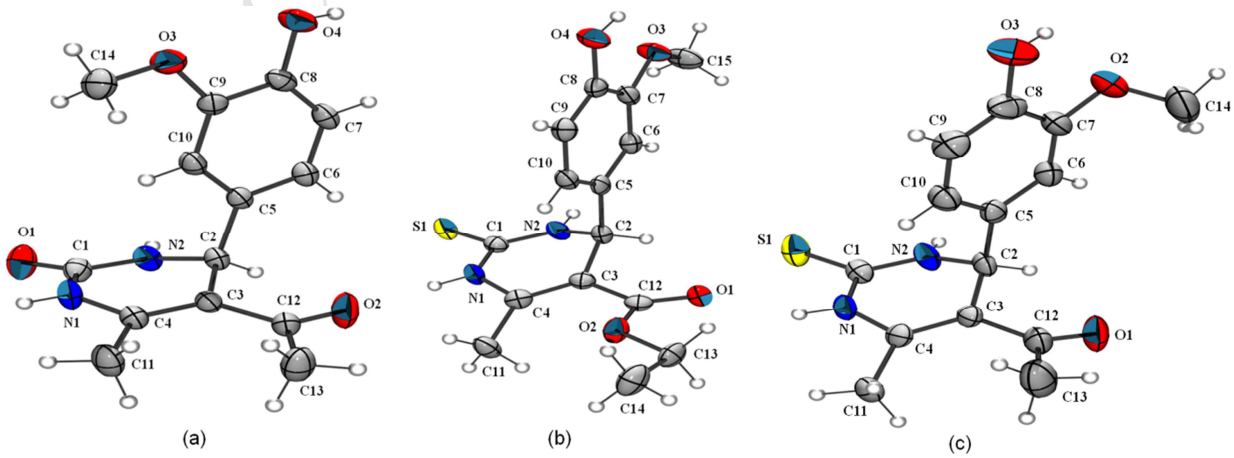

Figure 1. ORTEP diagram for (a) DHPM **I,** (b) DHPM **II** and (c) DHPM **III**. The ellipsoids are represented at 50% of probability, for (a) and (c), while (b) is shown at 80% of probability.

Table 1 shows the main crystallographic parameters. The principal torsion angles in order to describe the conformation differences among **I**, **II** and **III** are listed in Table 2. Table 3 lists the intermolecular interactions observed in all crystal structures. The main bond lengths and bond angles are depicted in Table S2.

Table 1. Crystallographic data and structure refinement for DHPM **I**, **II** and **III.**

Crystal data	**DHPM I**	**DHPM II**	**DHPM III**
Chemical formula	$C_{14}H_{16}N_2O_4$	$C_{15}H_{18}N_2O_4S$	$C_{14}H_{16}N_2O_3S$
Molecular weight	276.29	322.37	292.35
Space group	$P2_1/c$	$P\bar{1}$	$P2_1/c$
a, *b*, *c* (Å)	7.2339 (2), 14.9870 (4), 12.3278 (4)	8.4527 (2), 9.2867 (3), 11.0363 (3)	12.3080 (14), 7.1963 (8), 16.9759 (19)
α, β, γ (°)	90, 92.161 (3), 90	96.949 (1), 108.145 (1), 109.392 (1)	90, 109.185 (12), 90
V (Å^3)	1335.57 (7)	751.81 (4)	1420.1 (3)
Z	4	2	4
Radiation type	Mo *K*α	Cu *K*α	Mo Kα
μ (mm^{-1})	0.10	2.10	0.24
R [$F^2 > 2\sigma(F^2)$]	0.049	0.029	0.057
wR (F^2)	0.125	0.074	0.160
S	1.04	1.05	0.96
No. of reflections	3609	2539	4971
No. of parameters	185	203	187
$\Delta\rangle_{max}$, $\Delta\rangle_{min}$ (e Å^{-3})	0.28, -0.26	0.29, -0.34	0.26, -0.30

Table 2. Relevant experimental torsion angles (°) for DHPM **I**, **II** and **III**.

Torsion	**DHPM I**	**DHPM II**	**DHPM III**
C5–C2–C3–C12	-77.84 (14)	-80.55 (15)	-78.90 (4)
C5–C2–N2–C1	-98.78 (15)	-93.01 (15)	-94.10 (4)
C6–C5–C2–C3	122.87 (13)	167.12 (12)	137.70 (3)
C12–C3–C2–N2	156.86 (11)	156.11 (11)	157.30 (3)
C4–C3–C2–C5	102.62 (14)	99.29 (15)	100.60 (4)
N2–C2–C5–C10	65.60 (16)	106.82 (15)	79.40 (4)
C6–C5–C2–N2	-112.54 (14)	-70.11 (16)	-98.80 (4)
C10–C5–C2–C3	-59.00 (17)	-15.95 (19)	-44.10 (4)

The crystal packing of DHPM is formed by the polar sheets and the functional group (if it is involved in intermolecular interactions) present on the phenyl moiety (defined as ‘‘hydrophobic

spacer'') [16]. The DHPM **I** crystallized in the monoclinic system with space group $P2_1/c$ and Z=4 (Z'=1), which represents 4 molecules in the unit cell. The crystal packing of DHPM **I** is formed via strong hydrogen bonds and weak interactions, where there are three potential hydrogen bond donors, namely H1N, H2N, H4O and three potential acceptors, namely the carbonyl oxygen atom O1, the hydroxyl oxygen O2 and the methoxy oxygen O3, respectively. These crystal packing of DHPM **I** results in the formation of linear chain motifs utilizing $N_1–H_1N\cdots O_2$ hydrogen bonds, which can be described $\boldsymbol{C_1^1}(6)$, involving the ketone group generating strong motif in polar sheet along the *a* axis (Figure 2a). While chain motif utilizing $N_2–H_2N\cdots O_3$ hydrogen bonds (Figure 2b) are responsible by generating motif in hydrophobic space involving the methoxy group along the *c* axis, which can be described as $\boldsymbol{C_1^1}(7)$. Further, it is possible to observe an intermolecular hydrogen bond of $O_4–H_4O\cdots O_1$, the graph set is given as $\boldsymbol{C_1^1}(10)$, which results in the generation of a zig zag motif perpendicular to the *ab* plane (Figure 2c). Figure 2d shows the packing with the crystal structure, S and R configurations are shown in stick and wireframe style, respectively**.**

Table 3. Hydrogen-bond geometry (Å, °) for DHPM **I**, **II** and **III**.

DHPM	D–H···A	D–H	H···A	D···A	D–H···A	Symmetry code
I	N1–H1N···O2	0.86	2.07	2.903	164.00	-1+x,y,z
	N2–H2N···O3	0.86	2.26	3.110	168.00	x,1/2-y,-1/2+z
	O4–H4O···O1	0.82	1.94	2.759	175.00	1+x,1/2-y,1/2+z
II	N1–H1N···S1	0.86	2.56	3.389	162.00	-x,-y,-z
	N2–H2N···S1	0.86	2.48	3.312	163.00	1-x,-y,-z
	O4–H4O···O1	0.82	2.02	2.749	149.00	2-x,1-y,1-z
III	O3–H3O···O2	0.82	2.33	3.023	142.00	1-x,1-y,-z
	N2–H2N···S1	0.86	2.48	3.328	168.00	-x,2-y,-z
	N1–H1N···O1A	0.86	2.07	2.917	168.00	x,1+y,z

The packing diagram, in Figure 2, shows the motifs in the crystalline lattice**.** Previous studies have been performed on these packing motifs of these DHPM [33,34].

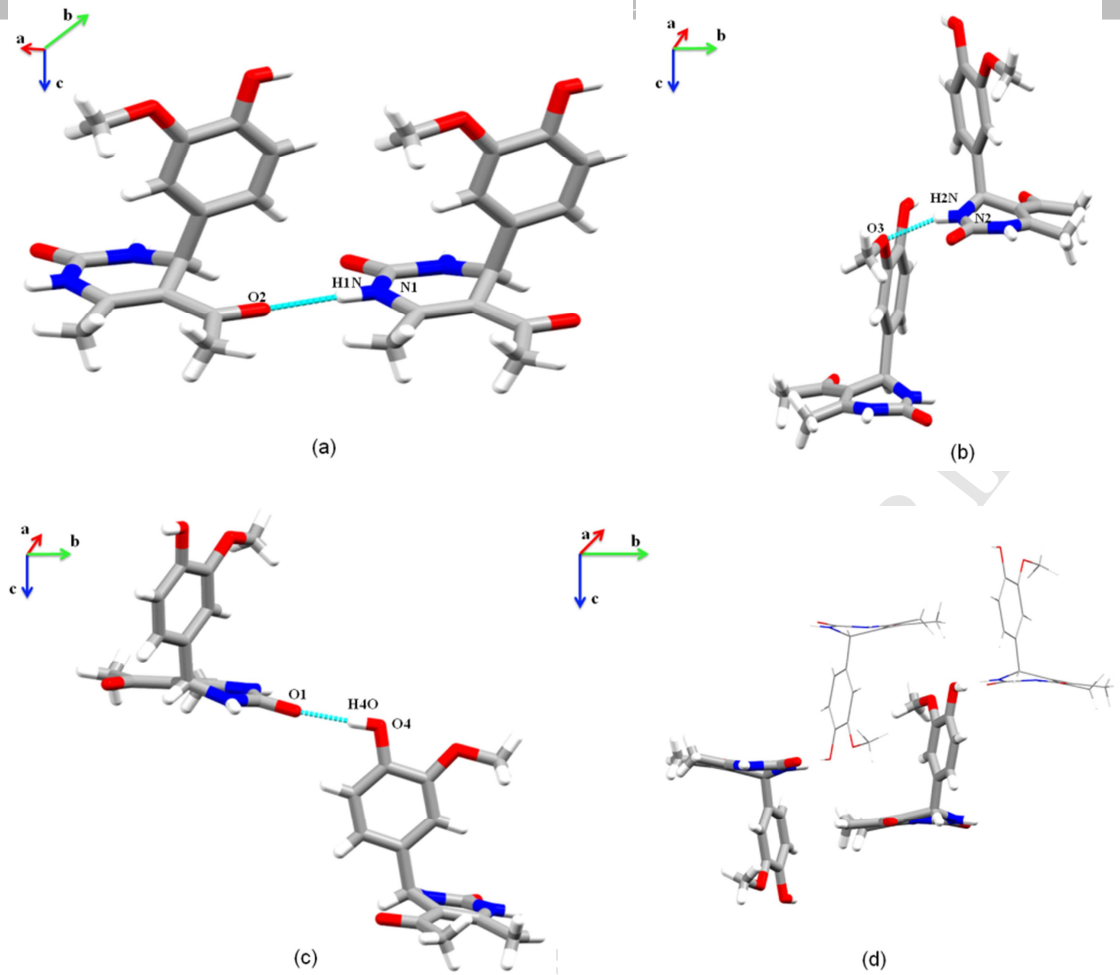

Figure 2. N–H···O (a and b) and O–H···O (c) intermolecular interactions and molecular packing (d) of DHPM **I**.

It was observed that the molecular conformational and packing features with theoretical calculation, powder diffraction and Raman did not study yet. It crystallizes in the triclinic system with space group $P\bar{1}$ and Z = 2, which represents two molecules in the unit cell. The crystal packing consists of N–H···S hydrogen bonded dimers form a $\mathbf{R_2^2}$ (8) [35-36] ring motif generating ribbons along the *a* axis (Figure 3a). The hydroxyl group participates in strong interaction O_4–H_4O···O_1 intermolecular hydrogen bonding generating dimers along the *c* axis, which can be described as $\boldsymbol{R_2^2}(8)$ (Figure 3b). Figure 3c shows the packing diagram with motifs in the crystal structure**.** DHPM **II** was characterized by X-ray powder diffraction and the results, shown in Figure S4, indicate that the entire sample crystallizes in a single phase.

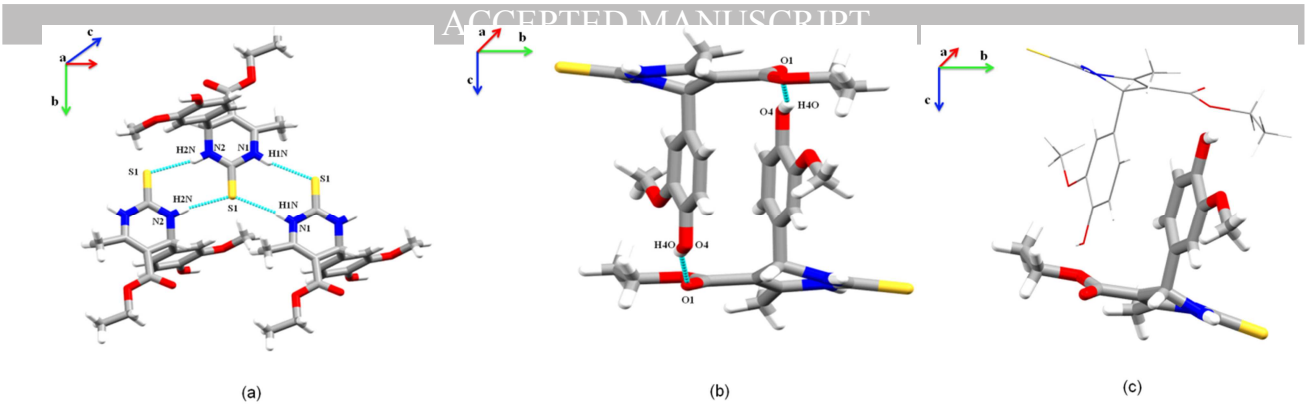

Figure 3. N–H···O (a and b) and O–H···O (c) intermolecular interactions and molecular packing (d) of DHPM **I**.

Similar to the DHPM **I**, the DHPM **III** crystallizes in the monoclinic system with space group $P2_1/c$ and Z=4. The oxygen atom O1 derived from methoxy group finds itself disordered in two occupation sites in the proportions 70:30. The crystal packing of DHPM **III** results in the formation of dimeric motifs utilizing O_3–H_3O···O_2 hydrogen bonds, which can be described $\boldsymbol{R_2^2}(10)$, involving the hydroxyl group generating strong motif in hydrophobic space (Figure 4a), while dimeric motif utilizing N_2–H_2N···S_1 hydrogen bonds (Figure 4b) are responsible by generating strong motif in polar sheets, which can be described as $\boldsymbol{R_2^2}(8)$. The intermolecular N_1-H_1N···O_{1A} hydrogen bonds, the graph set is given as $\boldsymbol{C_1^1}(6)$, link the molecules into polar sheet chains running along the *b* axis (Figure 4c). Figure 4d shows the packing with motifs in the crystal structure, S and R configurations are shown in stick and wireframe style, respectively**.** DHPM **III** was characterized by X-ray powder diffraction and the results, shown in Figure S5, indicate that the entire sample crystallizes in a single phase.

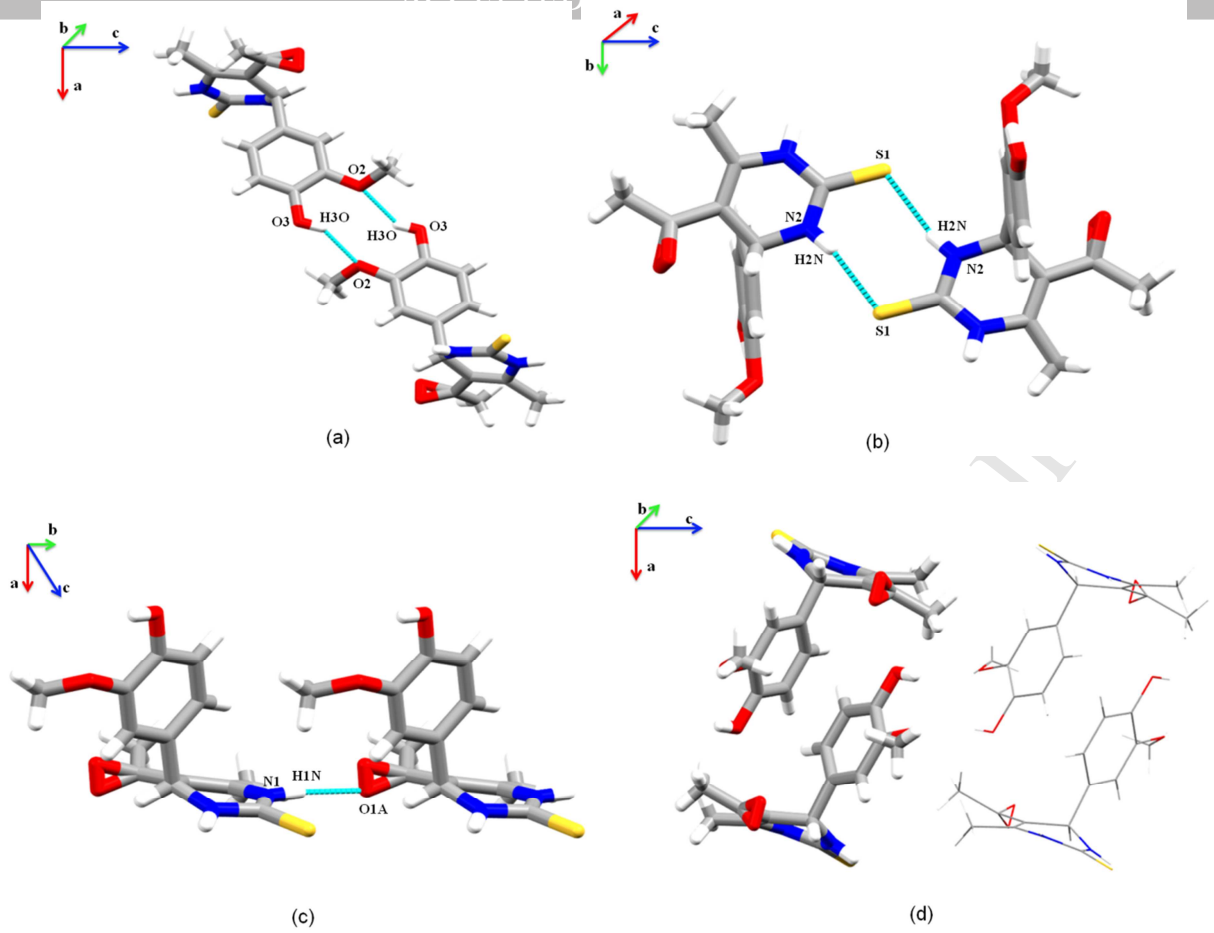

Figure 4. N–H···O (a and b) and O–H···O (c) intermolecular interactions and molecular packing (d) of DHPM **III**.

The HS mapped over $\boldsymbol{d_{norm}}$ (ranging from -0.511 to 1.470 Å) is shown in Figure 5. The red spot represent the H···O (15.7%) and O···H (18.5%) interactions of the DHPM **I** (Figure 5a). The N···H/H···N interactions result in the fingerprint plot (Figure 5b and 5c). This analysis is very helpful in the identification of the most dominant interactions among neighboring stacks [33]. In Figure 5d, the red spots represent the H···O (7.6%), O···H (9.0%), H···S (5.7%), S···H (9.3%) interactions of the DHPM **II**, whereas for the DHMP **III**, H···O (9.7%), O···H (10.9%) H···S (6.2%) and S···H (10.1%) interactions can be observed (Figure 5e). Such interactions are seen in the $\boldsymbol{d_e}$ and $\boldsymbol{d_i}$ surfaces of the molecule.

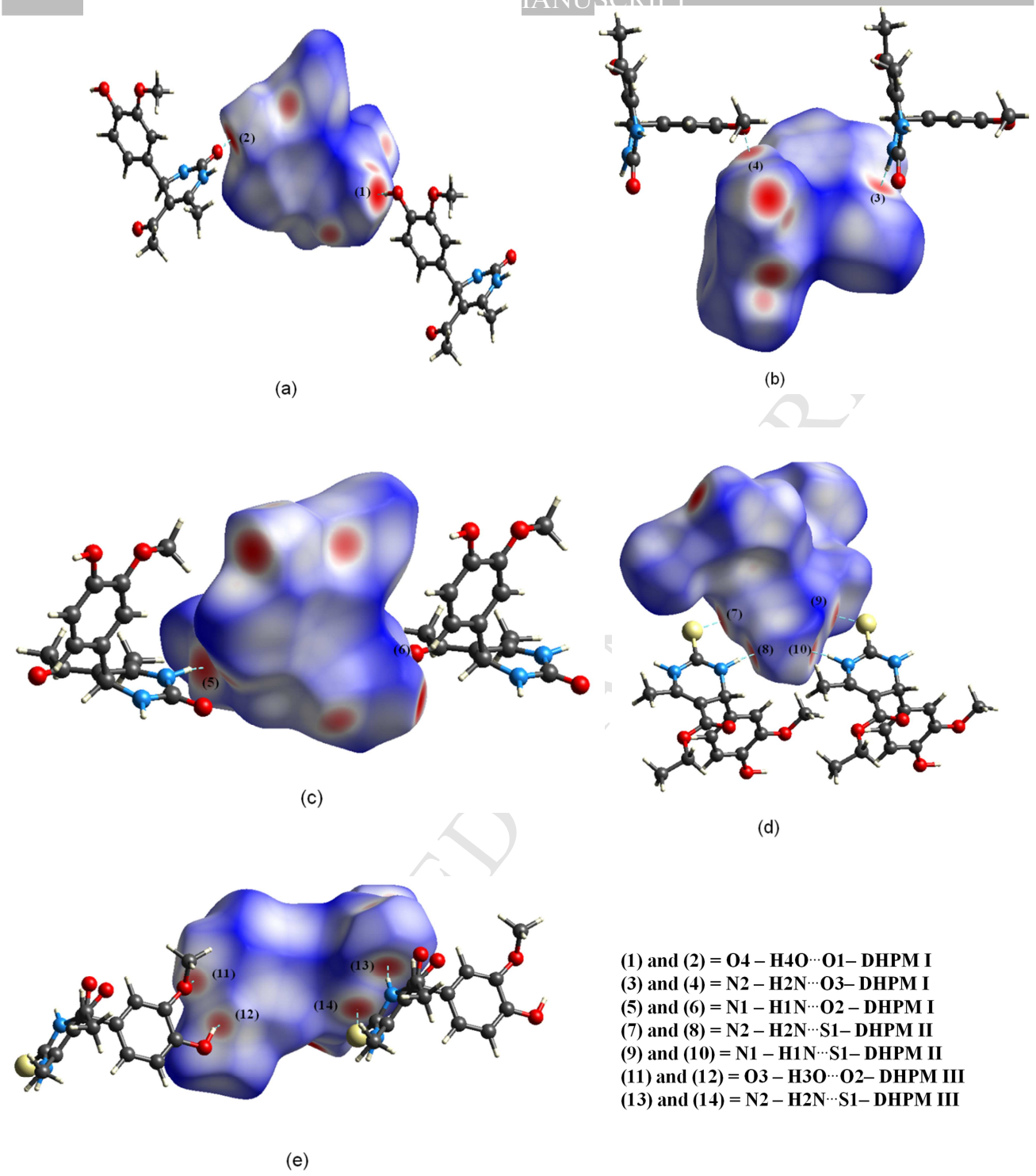

Figure 5. Hirshfeld surfaces ploted for DHPM **I** (a), (b) and (c); DHPM **II** (d) and DHPM **III** (e). Dotted lines were used to represent hydrogen bonds.

The shape index HS is an important tool to signal hydrophobic interactions (π···π and C–H···π interactions). The C–H···π interaction from DHPM **I,** formed by the center of aromatic ring characterized by C5–C10 (Cg1), is shown in Figure 6a and 6d. This interaction can be defined by

large red depressions above the aromatic ring. The π···π stacking shown in Figure 6b and 6e is displayed on shape index of DHPM **II** by red and blue triangles. Shape index refers to phenyl rings, which are maintained by hydrophobic Cg1–Cg1 interactions (the distance from one centroid to another is 3.494 Å) granting further stability for the structures. The effect of C–H···π interaction from DHPM **III** involving Cg1 are shown in Figure 6c and 6f.

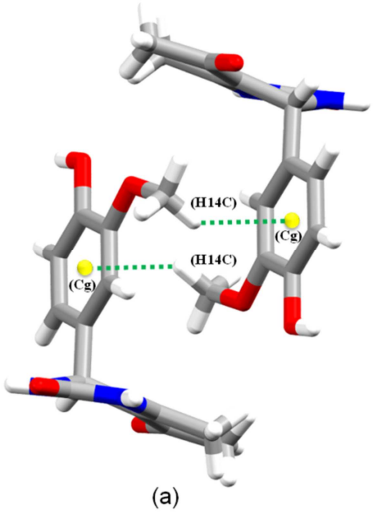

(a)

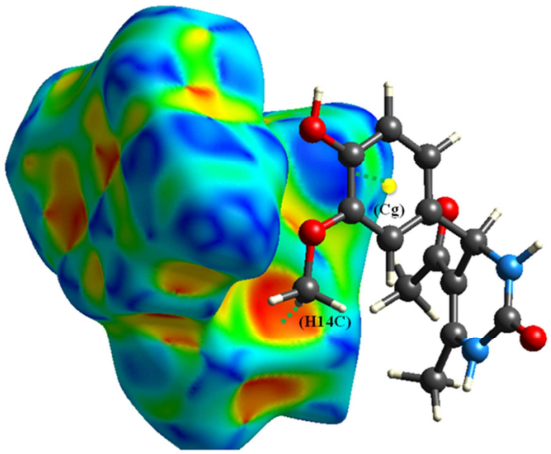

(d)

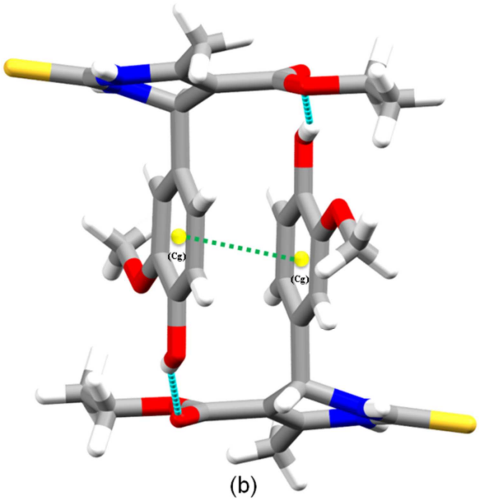

(b)

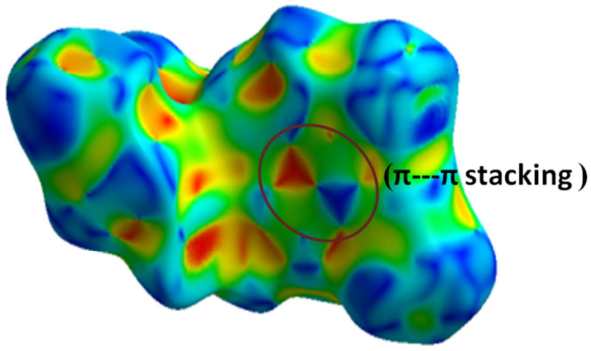

(e)

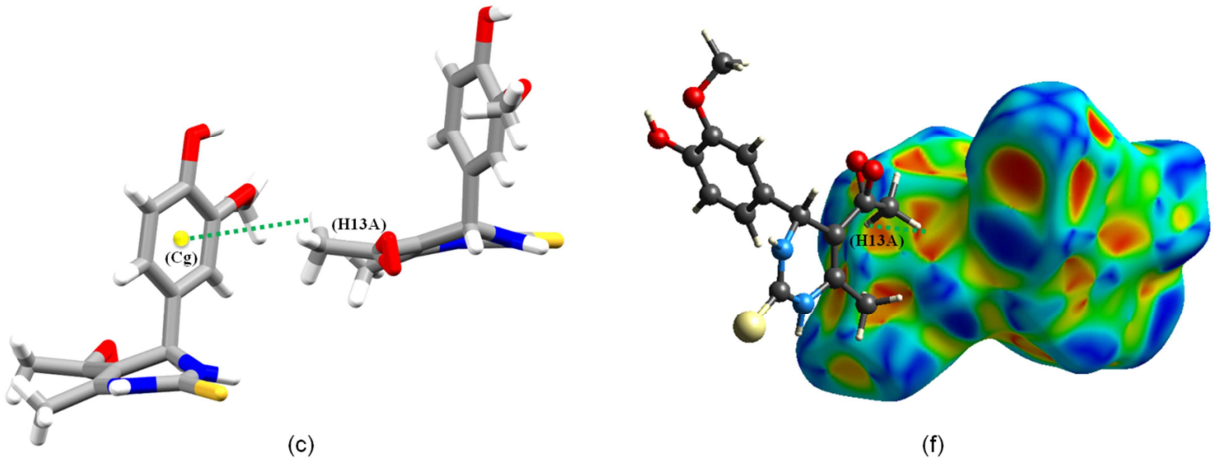

Figure 6. Representation of C–H···π and π···π interactions of DHPM **I** (a), **II** (b) and **III** (c). Shape index surfaces of DHPM **I** (d) and DHPM **III** (f) showing C–H···π interactions and DHPM **II** (e) evidencing π···π interactions.

Figure 7 displays the 2D fingerprint plots of DHPM **I**, **II** and **III**, where most of the contact is due to H···H interaction, which adds up to 43.0 %, 47.5% and 43.6% of the HS of DHPM **I**, **II** and **III** respectively. The contributions of O···H/H···O interactions, characterized by the spikes in the bottom of the fingerprint plot, represent 34.2%, 16,6% and 20.6% of the HS in the DHPM **I** (Figure 7a), **II** and **III** respectively. As for C···H/H···C interactions of DHPM **I, II** and **III**, it is observed 18.0%, 11.1% and 14.4% of the HS respectively. An important contribution of S···H/H···S interactions, characterized by wings observed at the left and right-side bottom for DHPM **II** and **III** (Figure 7c), reaches values of 16.6% and 16.3% of the HS, respectively. Another feature of DHPM **II** is the presence of C···C interactions, which is responsible for 2.8% of HS (Figure 7b).

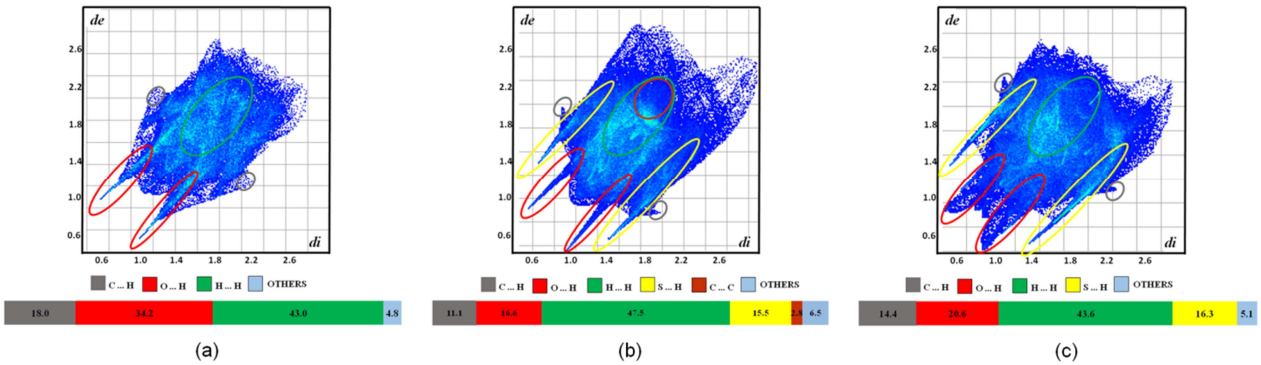

Figure 7. Fingerprint plots for DHPM **I** (a); DHPM **II** (b) and DHPM **III** (c).

The root of the mean squared (RMS) values, predicted using Mercury was 0.0189 for DHPM **I** and **II**, while for DHPM **I** and **III** was 0.0124. Further for DHPM **II** and **III** was 0.0211 as shown in Figure 8. The overlay of the tetrahydropyridimine ring is different in both the forms. The six-membered tetrahydropyrimidine ring exhibits a dihedral twist of 82.77^{o} with the aryl ring in DHPM **I**. For the DHPM **II**, the six-membered tetrahydropyrimidine ring exhibits a dihedral twist of 73.01^{o} with the aryl ring. The rings of tetrahydropyrimidine and aryl are approximately orthogonal to each other, the dihedral twist are at 89.76^{o} in DHPM **III**. DHPM **I**, **II** and **III** also differ by dihedral angles N2–C2–C5–C10, present in the tetrahydropyrimidine ring, the values are 65.60º, 106.82º and 79.30º, respectively (Table 2).

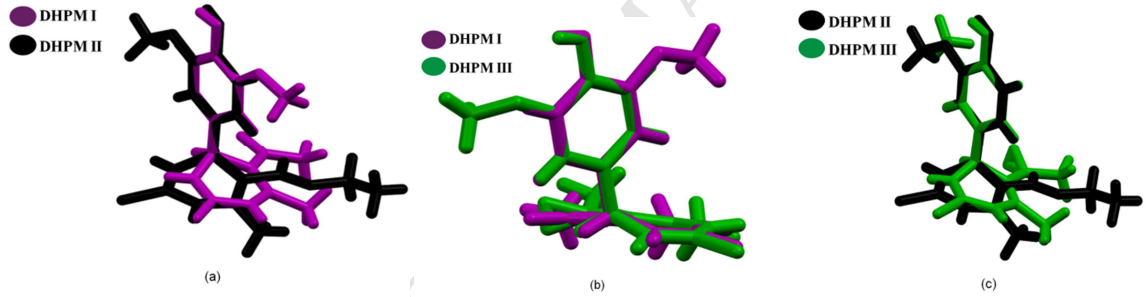

Figure 8. Overlay diagram of the molecular conformation in (a) DHPM **I** (purple), in (b) DHPM **II** (black) and (c) DHPM **III** (green) in respect to the aromatic ring.

A further comparison of DHPM **I** with DHPM **III** results in the formation of dimeric motif utilizing $N_2–H_2N^{\cdots}S_1$ hydrogen bonds and dimeric motifs being bridged by $O_3–H_3O^{\cdots}O_2$ intermolecular hydrogen bonds involving the hydroxyl group, that made an strong motif in hydrophobic space of DHPM **III**. Thus the crystal packing is different of DHPM **I** because of the participation of the hydroxyl group generating edge-to-edge motif in hydrophobic space. These intermolecular hydrogen bonds are responsible for the pre-organization of the DHPMs and contribute to the stability of the crystalline lattice. As a result of the delocalization of the lone pair of electrons from the nitrogen atoms N1 or N2 over the carbonyl group, the nitrogen and the oxygen

atoms assume considerable positive and negative charges, respectively [16]. The sulfur atom containing analogs of these Biginelli DHPM present similar behavior. The crystal structures object of this study can be divided into two different supramolecular arrangements. The first, formed by strong hydrogen bonds between polar functional groups, and the second built up using aryl ring moieties.

Molecular Modeling

The calculated geometries of DHPM **I** and **II** were compared to experimental model by structural overlapping (Figure 9) and the root of the mean squared deviation (RMSD) shows a good agreement in terms of interatomic distances and bond angles in DHPM **I**, **II** and **III**. The RMSD values are 0.0097, 0.0058 and 0.0090 for DHPM **I**, **II** and **III**, respectively, then DHPM **III** appears to have a more flexible set of intermolecular interactions than DHPM **I** and **II** since the DFT calculations consider the molecule in an environment free of interactions (gas phase).

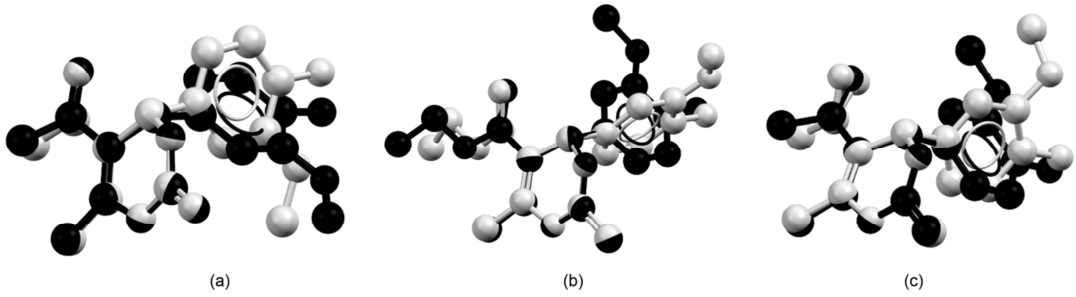

Figure 9. Overlapping of DFT (black) and X-ray (gray) structures from DHPM **I** (a), **II** (b) and **III** (c).

The HOMO and LUMO energy, obtained using DFT methods, was used to obtain some global reactivity descriptors (Table 4) to develop a better explaining of the stability and reactivity of DHPM **I**, **II** and **III**. In Figure 10 shows a graphical representation of HOMO and LUMO orbitals, in DHPM **I**, **II** and **III** the HOMO is located at aromatic ring while LUMO is spread at dihydropyrimidine ring.

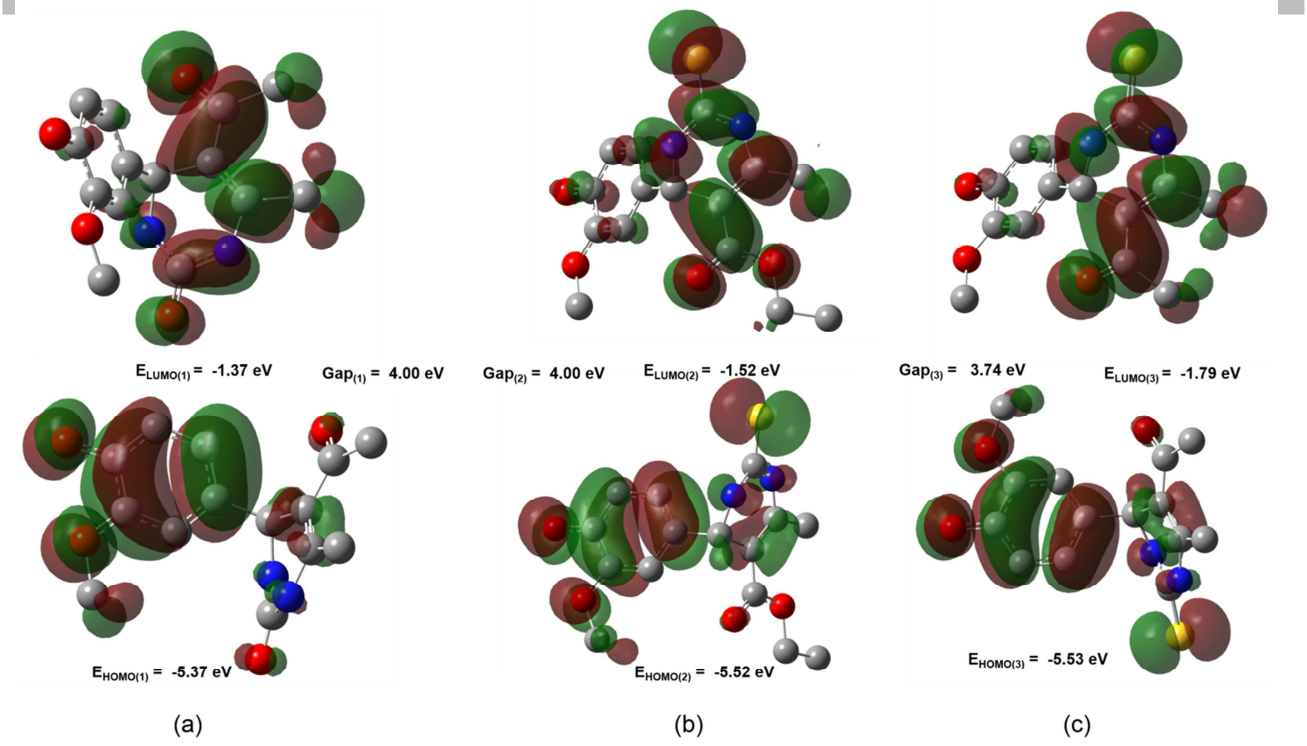

Figure 10. Theoretical HOMO-LUMO plots, energies and band gaps of DHPM **I** (a), **II** (b) and **III** (c).

The evaluation of the global indicators, inherent electronic property, of a set of DHPM **I**, **II** and **III** allows understand its potential for a chemical alteration and give good indexes to the explanation of the system [37]. The values presented in Table 4 were obtained using the same formulas proposed by DHANDAPANI et al. [33].

Table 4. The global reactivity descriptors of DHPM **I**, **II** and **III**.

Molecular properties	**I**	**II**	**III**
Ionization potential (I)	5.37	5.52	5.53
Electron affinity (A)	1.37	1.52	1.79
Chemical potential (μ)	-3.37	-3.52	-3.66
Global hardness (η)	2.00	2.00	1.87
Softness (s)	0.50	0.50	0.53
Energy gap (eV)	4.00	4.00	3.74
Electrophilicity index (ω)	2.84	3.10	3.58
Dipole moment (Debye)	3.67	6.53	5.59

The transfer of electrons between two molecules is driven by differences in chemical potential, the values obtained in this study show a decreasing order of reactivity as DHPM **III**

(more reactive), **II** and **I** respectively. On the other hand, hardness could be understood like the resistance of a system to transfer its charge, DHPM **I** and **II** has the same value while DHPM **III** presents to be the easiest system to suffer transfer charge. In terms of electrophilicity the calculated values determine that DHPM **III** is the most disposed of accept electrons from the outside environment, that is a good electrophile, while the lower value of DHPM **I** indicates that as a good nucleophilic species.

To understand the potential electrophilic and nucleophilic sites in DHPM **I**, **II** and **III** were used the 3D MEP representation (Figure 11). In general, it is seen that the negative potential regions (red), susceptible to electrophilic attack, are mostly limited over the oxygen atoms, moreover, in DHPM **II** and **III** that appears over sulfur atoms too. On the other hand, positive regions (blue), susceptible to nucleophilic attack, are restricted around hydrogen atoms of aromatic rings and nitrogen atoms. This pattern is like that expressed involving that class of DHPM [33,38,39].

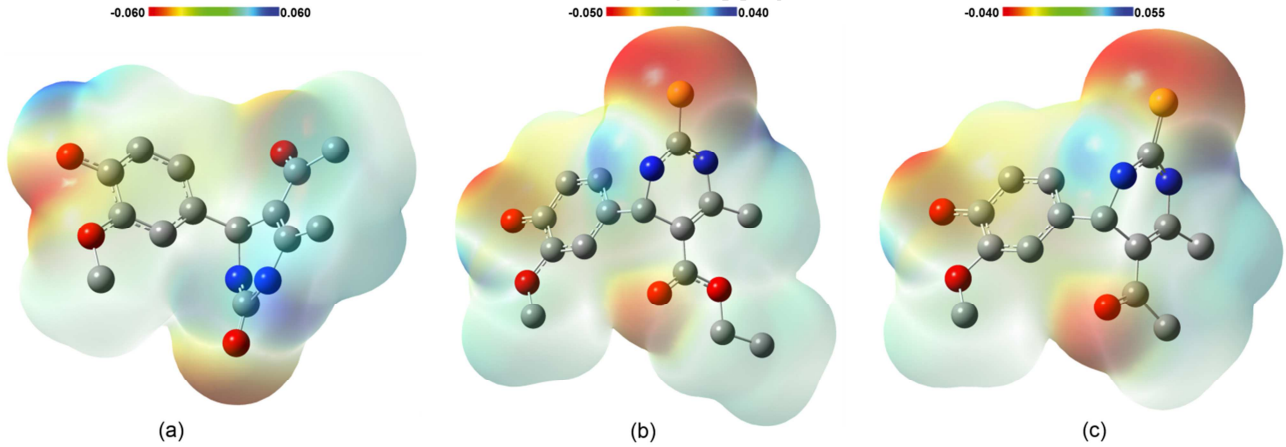

Figure 11. Molecular electrostatic potential maps of DHPM **I** (a), **II** (b) and **III** (c). The energy range for each surface is show above it.

The experimental and calculated FT-IR spectra are shown in Figure 12 and the assigned vibrational modes of main groups of DHPM **I**, **II** and **III** are proposed in Table 5. In Figure**s** S6, S7 and S8, it are possible seen the main assignments to Raman spectra for DHPM **I, II** and **III**. To correct the systematic overestimation by DFT methods in vibrational frequencies these values were scaled by 0.962.

Table 5. Theoretical and experimental vibrational assignments for DHPM **I**, **II** and **III**.

	DHPM I		**DHPM II**		**DHPM III**	
Vibrational mode	Scaled Freq[a,b].	Exp. Freq[b].	Scaled Freq[a,b].	Exp. Freq.[b]	Scaled Freq[a,b].	Exp. Freq.[b]
ν $(C=C)_{Ar}$	1596; 1591	1613; 1527	1604; 1593	1589; 1519	1603; 1592	1504; 1456
ν C=C	1606	1608	1615	1587	1605	1587
ν C=O	1757; 1650	1691; 1638	1682	1685	1648	1629
ν N-H	3508-3492	3293	3504-3492	3181	3499	3293
ν O-CH_3	1294	1331	1228	1235	1266	1270
ν O-H	3678	3350	3625	3416	3625	3468
ν CH_3	3005-2899	2971-2934	3010-2910	2842	3008-2912	2945-2841

ν= stretching; a) Scale factor 0.962; b) cm^{-1}

For experimental spectra for DHPM **I**, it is possible noted two bands, at 1691 and 1638 cm^{-1}, which are related to νC=O in heterocyclic and from the group in alkyl fraction, respectively. Theoretical vibrational modes occur at 1757 cm^{-1} and at 1650 cm^{-1}, in relation to experimental data. In experimental Raman scattering, this bands occur with moderate intensity at 1685 cm^{-1} and at 1642 cm^{-1}. For infrared data of the DHPM **II**, this mode appears at 1685 cm^{-1} experimentally and at 1682 cm^{-1} theoretically, where the νC=O belongs to ester group, while in DHPM **III**, this value is at 1629 cm^{-1} (experimental) and at 1648 cm^{-1} (DFT). For the Raman data for DHPM **II** and DHPM **III**, it presents values of 1673 cm^{-1} and 1627 cm^{-1}, respectively, referring to the C=O bond.

The stretching vibration in the spectra of vinyl group occurs at 1660–1600 cm^{-1} and, in case of conjugation, just like in DHPM **I**, **II** and **III**, it could be moved to lower frequencies [40]. In DHPM **I** the presence of an infrared absorption band at 1608 cm^{-1} and a calculated at 1606 cm^{-1} indicate the νC=C mode, and it shows up in experimental Raman as a band of strong intensity at 1603 cm^{-1}, while in DHPM **II** and **III** these values are 1615 cm^{-1} and 1605 cm^{-1}, for experimental infrared spectra. In experimental Raman spectra it shows at 1607 cm^{-1} for DHPM **II** and at 1606 cm^{-1} for DHPM **III**. Theoretical infrared spectra for DHPM **II** and **III** display absorption bands at 1587 cm^{-1}. The stretch C=C of an aromatic ring often occur [40] in pairs at 1600 to 1475 cm^{-1}. Experimentally these absorptions appear at 1613, 1527 cm^{-1} (for DHPM **I**), 1589, 1519 cm^{-1} (for DHPM **II**), 1504 and 1456 cm^{-1} (for DHPM **III**) while, theoretically, these values are 1596 cm^{-1}, 1591 cm^{-1}, 1604 cm^{-1}, 1593 cm^{-1}, 1603 cm^{-1} and 1592 cm^{-1}, respectively. Experimental data for

Raman scattering shows this bands at 1469 cm^{-1} and 1522 cm^{-1} for DHPM **I** and at 1569 cm^{-1} and 1478 cm^{-1} for DHPM **II**, whereas for DHPM **III**, this scattering bands show at 1586 cm^{-1} and 1463 cm^{-1}.

The methoxy stretching vibration, when it is attached to an aromatic ring, appears at the region [40] of 1310-1210 cm^{-1}, experimental infrared spectra shows absorption peaks at 1331, 1235 and 1270 cm^{-1} for DHPM **I**, DHPM **II**, DHPM **III**, respectively. On the other hand, theoretical peaks appear at 1294, 1228 and 1266 cm^{-1}, respectively. For DHPM **I**, experimental Raman spectra shows peaks at 1327, 1290 and 1240 cm^{-1}, which are attributed to methoxy stretching vibration. For DHPM **II**, it shows up at 1373, 1330 and 1250 cm^{-1} and for DHPM **III** in at 1331, 1274 and 1249 cm^{-1}.

The position of νO–H band, for primary phenols, appears around at 3630 cm^{-1}, but intermolecular hydrogen bonding weakens it, so shifting the band to lower frequency [40]. DFT calculations assign the νO–H band at 3678 cm^{-1} for DHPM **I** and at 3625 cm^{-1} for DHPM **II** e **III** while experimental bands are shifted to lower frequencies, due O···H interactions, at 3350, 3416 and 3468 cm^{-1}, respectively.

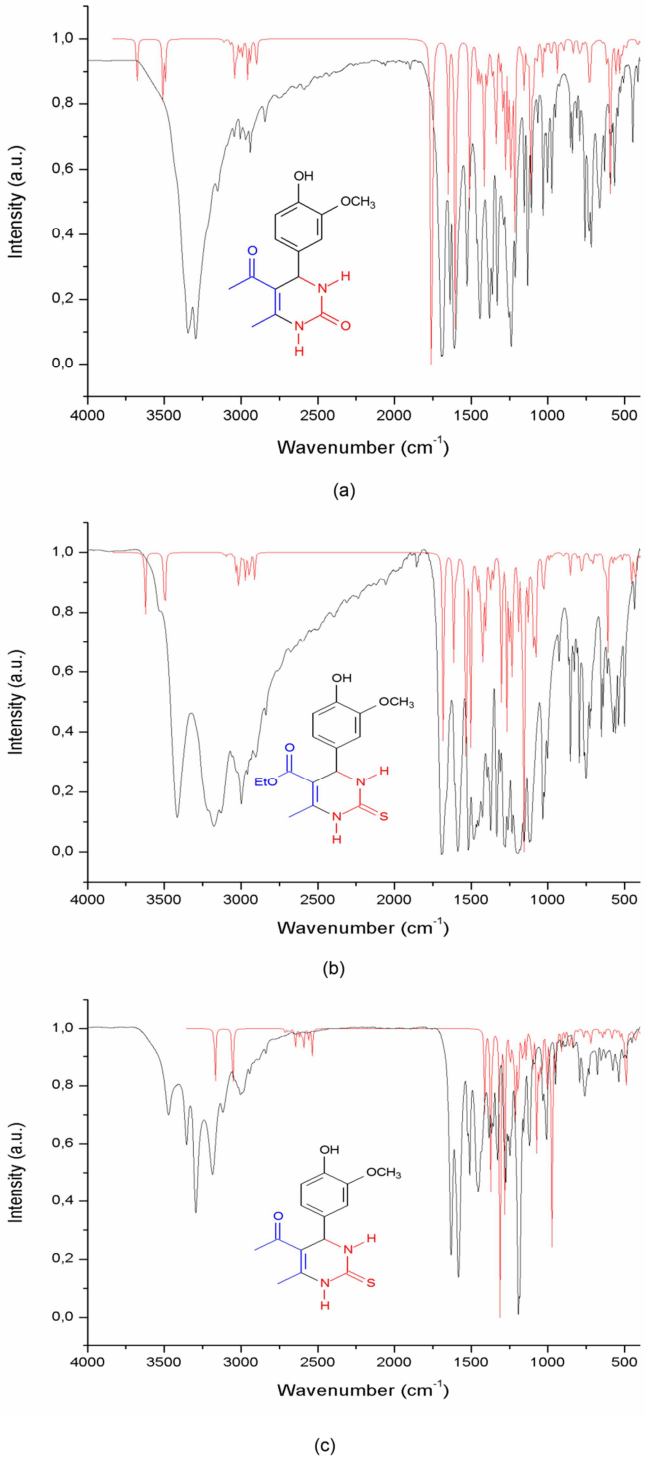

Figure 12. Experimental (black) and theoretical (red) overlapped FT-IR spectrum of DHPM **I** (a), **II** (b) and **III** (c).

The DHPM **I** studied in this work showed inhibitory activity against L3MBTL1 (IC_{50} = 89.1 nM [41]. L3MBTL1 is a protein "readers" of the histone code and play an important role in the epigenetic regulation of gene expression, depletion of L3MBTL1 may trigger defects in DNA

replication [42]. It was also observed that the L3MBTL1 gene is situated in a region normally erased in a few myeloid malignancies, including intense myeloid leukemia [43]. These facts suggest L3MBTL1 as a supposed tumor suppressor protein. L3MBTL1, belongs to a group of factor containing malignant brain tumor (MBT) repeats having a tandem repeat of three MBT domains (Figure 14). It is noteworthy that only the second MBT domain has been shown to bind to methylated histone peptides [44]. We chose MBT2 repeat for our molecular docking research aimed at to propose new promising ligands of L3MBTL1. The docking protocol was tested by redocking process to reproduce the binding mode of the co-crystal structure (PDB code: 3P8H). The docking protocol we employed predicted a similar conformation with a RMSD value of 0.76 Å. In redocking simulations, RMSD, less than 2 Å validates a docking protocol [45,46]. Figure 13 shows how the ligand 3-bromo-5-[(4-pyrrolidin-1-ylpiperidin-1-yl)carbonyl]pyridine (P8H) bound to the L3MBTL1 MBT2 repeat analogous to the co-crystallized ligand. This shows that the parameters used are consistent for the study of DHPM **I**, **II** and **III** capable of interacting with the same region of the protein.

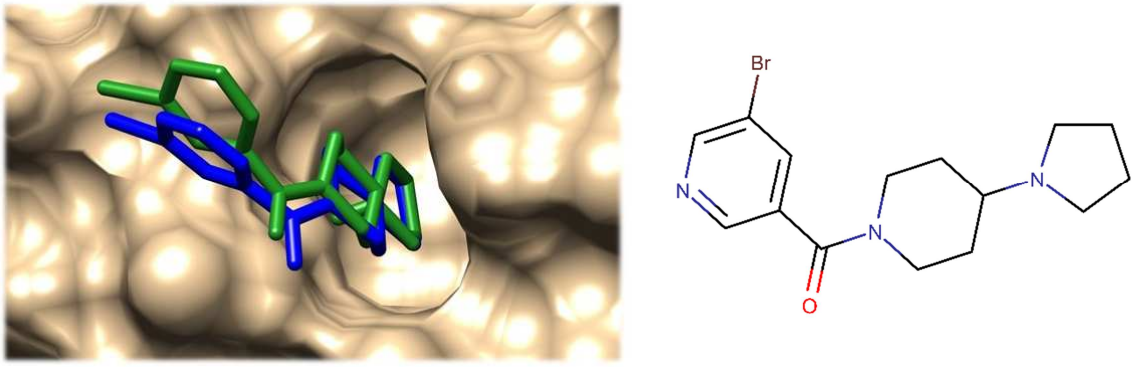

Figure 13. Redocking of co-crystallized ligand P8H (0.76 Å) inside MBT2 repeat (PDB code: 3P8H). Superposition between co-crystallized in *blue* and the best docking pose predicted in *green* with the protein surface. The two-dimensional representation is showed on the right-hand side. Molecular graphic was performed with the UCSF Chimera package.

Human L3MBTL1 has a deep, narrow pocket in the MBT2 domain. P8H ligand binds to this pocket via hydrogen bonding (1.72 Å) with Asp355 residue and Cation···π and π···π stacking

interactions with Tyr386 and Trp382 residues. This ligand was recently discovered as an inhibitor of L3MBTL1 (IC_{50} = 6μM) [47]. Using the same docking protocol our DHPM **I**, **II** and **III** were submited to molecular docking analysis into the L3MBTL1 structure (PDB code: 3P8H). After docking procedures the DHPM **I**, **II** and **III** were ranked and the best results were found out by the AutoDock Vina score. The interactions between DHPM **I**, **II** and **III** and the MBT2 repeat, reveal that some key amino acids residues, such as Asn358, Leu361, Cys363, Trp382, Tyr386 and Asp 355, make good contacts, see Figure 14. The residue Asn358 forms H-bonding with DHPM **I**, **II** and **III**, beyong to residue Asp355 forming the same hydrogen bond with the DHPM **II** like with the P8H ligand. Due the chemical similarity DHPM **I**, **II** and **III** interacts with Tyr386 and Trp382 residues by π···π stacking interactions. The ethoxy group of DHPM **II** forms hydrophobic interactions with Met357. Hydrophobic contacts are also observed between the DHPM **I** and Phe379. The S and O atoms in X position showed no interactions change. The DHPM **II** exhibited the best interactions in MBT2.

The binding mode predicted by docking simulations was extremely valuable for investigating the interactions between the DHPM **I**, **II** and **III** portrayed in this article and the human Lethal (3) malignant brain tumor-like protein 1, the outcomes recommends the DHPM **II** and **III** as potential candidates to L3MBTL1 inhibitors. Their results provided significant information for the design and synthesis of novel L3MBTL1 inhibitors. The improvement of potent L3MBTL1 inhibitors would fill as probes to more prominent comprehension the funcional role of this protein.

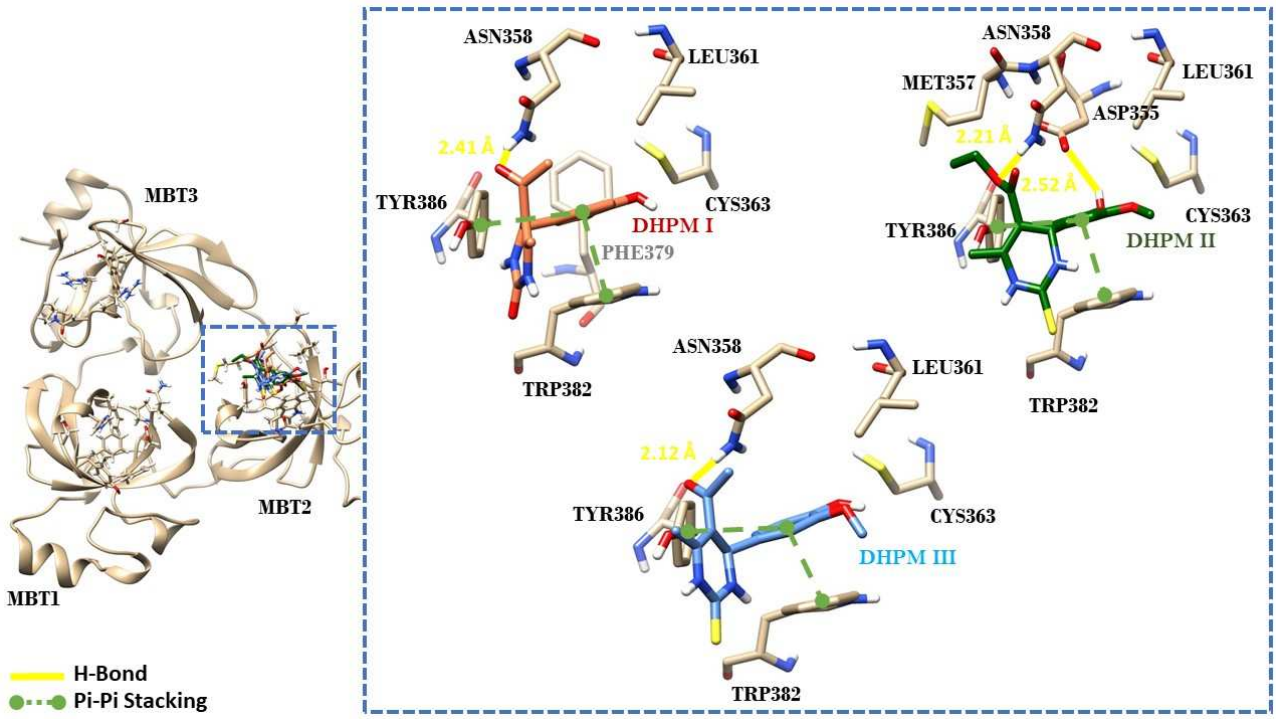

Figure 14. Docking results for DHPM **I**, **II** and **III** inside the MBT2 of L3MBTL1 crystallography structure (PDB code: 3P8H).

Conclusions

In this research we describe the synthesis and characterization of 5-acetyl-3,4-dihydro-4-(4-hydroxy-3-methoxyphenyl)-6-methyl-2(1*H*)-pyrimidinone (DHPM **I**), Ethyl-4-(4-hydroxy-3-methoxyphenyl)-6-methyl-2-thioxo-1,2,3,4-tetrahydropyrimidine-5-carboxylate (DHPM **II**) and 1-[1,2,3,4-tetrahydro-4-(4-hydroxy-3-methoxyphenyl)-6-methyl-2-thioxo-5-pyrimidinyl]-ethanone (DHPM **III**). X-ray diffraction data confirmed, in all DHPM, that the ester moiety appears in an s-cis configuration. The hydrogen bonds interactions originate different structural arrangements, which are the chains, dimers and ribbon formations along with the entire crystal packing. A broad vibrational analysis of DHPM **I**, **II** and **III** were done by B3LYP functional associated to 6-31G(d,p) basis set. The frontier molecular orbital analysis show that the three compounds has practically the same reactivity, being DHPM **III** slightly reactive. In a general way, the vibrational wavenumbers analysis show good correspondence with experimental data. Moreover, theoretical

calculations DHPM **III** as good electrophile, while DHPM **I** is the best nucleophilic species. In addition, MEP analysis reveals that the regions near to oxygen and sulfur atoms are the most susceptible to electrophilic attack. Molecular docking was successful used to predict the three novel pyrimidine derivatives binding modes. The results suggest the DHPM **II** and **III** as potential candidates to L3MBTL1 inhibitors.

Acknowledgements

The authors are grateful to the Coordenação de Aperfeiçoamento de Pessoal de Nível Superior (CAPES), Financiadora de Estudos e Projetos (FINEP), Conselho Nacional de Desenvolvimento Científico e Tecnológico (CNPq) and the Fundação de Amparo à Pesquisa do Estado de Goiás (FAPEG) for financial support. This research was developed with the support of the High Performance Computation Nucleus of UEG, State University of Goiás (UEG). Single crystal X-ray diffraction data were collected at Physics Institute of Federal University of Santa Catarina (UFSC) and Chemistry Department at Federal University of Juiz de Fora (UFJF).

References

[1] M.M. Karelson, A.R. Katritzky, M. Szafran, M.C. Zerner, Quantitative Predictions of Tautomeric Equilibria for 2-, 3-, and 4-Substituted Pyridines in both the Gas Phase and Aqueous Solution: Combination of AM1 with Reaction Field Theory, J. Org. Chem. 54 (1989) 6030–6034. doi:10.1021/jo00287a012.

[2] C.O. Kappe, Biologically active dihydropyrimidones of the Biginelli-type--a literature survey., Eur. J. Med. Chem. 35 (2000) 1043–1052. doi:S0223523400011892 [pii].

[3] C.O. Kappe, The Biginelli Reaction, in: Multicomponent React., 2005: pp. 95–120. doi:10.1002/3527605118.ch4.

[4] B.S. Holla, B.S. Rao, B.K. Sarojini, P.M. Akberali, One pot synthesis of thiazolodihydropyrimidinones and evaluation of their anticancer activity, Eur. J. Med. Chem. 39 (2004) 777–783. doi:10.1016/j.ejmech.2004.06.001.

[5] G. Kour, M. Gupta, S. Paul, Rajnikant, V.K. Gupta, SiO2-CuCl2: An efficient and recyclable heterogeneous catalyst for one-pot synthesis of 3,4-dihydropyrimidin-2(1H)-ones, J. Mol. Catal. A Chem. 392 (2014) 260–269. doi:10.1016/j.molcata.2014.05.022.

[6] A. Shaabani, M. Seyyedhamzeh, A. Maleki, F. Hajishaabanha, Diketene as an alternative substrate for a new Biginelli-like multicomponent reaction: one-pot synthesis of 5-carboxamide substituted 3,4-dihydropyrimidine-2(1H)ones, Tetrahedron. 66 (2010) 4040–4042. doi:10.1016/j.tet.2010.04.028.

[7] L. Saher, M. Makhloufi-Chebli, L. Dermeche, B. Boutemeur-Khedis, C. Rabia, A.M.S. Silva, M. Hamdi, Keggin and Dawson-type polyoxometalates as efficient catalysts for the synthesis of 3,4-dihydropyrimidinones: Experimental and theoretical studies, Tetrahedron Lett. 57 (2016) 1492–1496. doi:10.1016/j.tetlet.2016.02.077.

[8] K. Gong, H. Wang, S. Wang, X. Ren, β-Cyclodextrin-propyl sulfonic acid: A new and eco-friendly catalyst for one-pot multi-component synthesis of 3,4-dihydropyrimidones via Biginelli reaction, Tetrahedron. 71 (2015) 4830–4834. doi:10.1016/j.tet.2015.05.028.

[9] R. Kaur, S. Chaudhary, K. Kumar, M.K. Gupta, R.K. Rawal, Recent synthetic and medicinal perspectives of dihydropyrimidinones: A review, Eur. J. Med. Chem. 132 (2017) 108–134. doi:10.1016/j.ejmech.2017.03.025.

[10] H. Bienayme, C. Hulme, G. Oddon, P. Schmitt, Maximizing synthetic efficiency: multi-component transformations lead the way, Chem. - A Eur. J. 6 (2000) 3321–3329. doi:10.1002/1521-3765(20000915)6:18<3321::aid-chem3321>3.0.co;2-a.

[11] S. Chitra, D. Devanathan, K. Pandiarajan, Synthesis and in vitro microbiological evaluation of novel 4-aryl-5-isopropoxycarbonyl-6-methyl-3,4-dihydropyrimidinones, Eur. J. Med. Chem. 45 (2010) 367–371. doi:10.1016/j.ejmech.2009.09.018.

[12] A. Kamal, M. Shaheer Malik, S. Bajee, S. Azeeza, S. Faazil, S. Ramakrishna, V.G.M. Naidu, M.V.P.S. Vishnuwardhan, Synthesis and biological evaluation of conformationally flexible as well as restricted dimers of monastrol and related dihydropyrimidones, Eur. J. Med. Chem. 46 (2011) 3274–3281. doi:10.1016/j.ejmech.2011.04.048.

[13] W.M.F.F. and M.A.S. C. Oliver Kappe*, Calcium-channel modulators for cardiovascular disease., Tetrahedron. 53 (1997) 2803–2816. doi:10.1016.

[14] D. Subhas Bose, M. Sudharshan, S.W. Chavhan, New environmentally benign protocol for the synthesis of 3,4-dihydropyrimidin-2(1H)-ones: Practical access to mitotic kinesin EG5 inhibitor Monastrol, Arkivoc. 2005 (2005) 228. doi:10.3998/ark.5550190.0006.325.

[15] J.M. Blacquiere, O. Sicora, C.M. Vogels, M. Čuperlović-Culf, A. Decken, R.J. Ouellette,

S.A. Westcott, Dihydropyrimidinones containing boronic acids, Can. J. Chem. 83 (2005) 2052–2059. doi:10.1139/v05-211.

[16] S.K. Nayak, K.N. Venugopala, D. Chopra, T.N.G. Row, Insights into conformational and packing features in a series of aryl substituted ethyl-6-methyl-4-phenyl-2-oxo-1,2,3,4-tetrahydropyrimidine-5- carboxylates, CrystEngComm. 13 (2011) 591–605. doi:10.1039/c0ce00045k.

[17] L.M. Ramos, B.C. Guido, C.C. Nobrega, J.R. Corrêa, R.G. Silva, H.C.B. De Oliveira, A.F. Gomes, F.C. Gozzo, B.A.D. Neto, The biginelli reaction with an imidazolium-tagged recyclable iron catalyst: Kinetics, mechanism, and antitumoral activity, Chem. - A Eur. J. 19 (2013) 4156–4168. doi:10.1002/chem.201204314.

[18] G.M. Sheldrick, Crystal structure refinement with SHELXL, Acta Crystallogr. Sect. C Struct. Chem. 71 (2015) 3–8. doi:10.1107/S2053229614024218.

[19] L.J. Farrugia, WinGX and ORTEP for Windows: An update, J. Appl. Crystallogr. 45 (2012) 849–854. doi:10.1107/S0021889812029111.

[20] C.F. Macrae, P.R. Edgington, P. McCabe, E. Pidcock, G.P. Shields, R. Taylor, M. Towler, J. Van De Streek, Mercury: Visualization and analysis of crystal structures, J. Appl. Crystallogr. 39 (2006) 453–457. doi:10.1107/S002188980600731X.

[21] A.L. Spek, Structure validation in chemical crystallography, Acta Crystallogr. Sect. D Biol. Crystallogr. 65 (2009) 148–155. doi:10.1107/S090744490804362X.

[22] A.D. Martin, J. Britton, T.L. Easun, A.J. Blake, W. Lewis, M. Schröder, Hirshfeld surface investigation of structure-directing interactions within dipicolinic acid derivatives, Cryst. Growth Des. 15 (2015) 1697–1706. doi:10.1021/cg5016934.

[23] M.A.S. S.K. Wolff, D.J. Grimwood, J.J. McKinnon, M.J. Turner, D. Jayatilaka, CrystalExplorer (Version 3.1), Univ. West. Aust. (2012).

[24] M.J. Frisch, G.W. Trucks, H.B. Schlegel, G.E. Scuseria, M.A. Robb, J.R. Cheeseman, G. Scalmani, V. Barone, B. Mennucci, G.A. Petersson, H. Nakatsuji, M. Caricato, X. Li, H.P. Hratchian, A.F. Izmaylov, J. Bloino, G. Zheng, J.L. Sonnenberg, M. Hada, M. Ehara, K. Toyota, R. Fukuda, J. Hasegawa, M. Ishida, T. Nakajima, Y. Honda, O. Kitao, H. Nakai, T. Vreven, J.A. Montgomery Jr., J.E. Peralta, F. Ogliaro, M. Bearpark, J.J. Heyd, E. Brothers, K.N. Kudin, V.N. Staroverov, R. Kobayashi, J. Normand, K. Raghavachari, A. Rendell, J.C. Burant, S.S. Iyengar, J. Tomasi, M. Cossi, N. Rega, J.M. Millam, M. Klene, J.E. Knox, J.B. Cross, V. Bakken, C. Adamo, J. Jaramillo, R. Gomperts, R.E. Stratmann, O. Yazyev, A.J. Austin, R. Cammi, C. Pomelli, J.W. Ochterski, R.L. Martin, K. Morokuma, V.G. Zakrzewski, G.A. Voth, P. Salvador, J.J. Dannenberg, S. Dapprich, A.D. Daniels, Ö. Farkas, J.B. Foresman, J. V Ortiz, J. Cioslowski, D.J. Fox, Gaussian 09, Revision A.02, Gaussian Inc Wallingford CT. 34 (2009) Wallingford CT. doi:10.1159/000348293.

[25] R.D. Johnson III, NIST Computational Chemistry Comparison and Benchmark Database., NIST Stand. Ref. Database Number 101. (2018). doi:Release 19.

[26] M.H. Jamroz, Vibrational Energy Distribution Analysis VEDA 4, Warsaw, 2004.

[27] O. Trott, A.J. Olson, AutoDock Vina: improving the speed and accuracy of docking with a new scoring function, efficient optimization, and multithreading., J. Comput. Chem. 31 (2010) 455–61. doi:10.1002/jcc.21334.

[28] H.M. Berman, J. Westbrook, Z. Feng, G. Gilliland, T.N. Bhat, H. Weissig, I.N. Shindyalov, P.E. Bourne, The Protein Data Bank., Nucleic Acids Res. 28 (2000) 235–42. http://www.ncbi.nlm.nih.gov/pubmed/10592235 (accessed September 12, 2018).

[29] E.F. Pettersen, T.D. Goddard, C.C. Huang, G.S. Couch, D.M. Greenblatt, E.C. Meng, T.E.

Ferrin, UCSF Chimera?A visualization system for exploratory research and analysis, J. Comput. Chem. 25 (2004) 1605–1612. doi:10.1002/jcc.20084.

[30] J.A. Maier, C. Martinez, K. Kasavajhala, L. Wickstrom, K.E. Hauser, C. Simmerling, ff14SB: Improving the Accuracy of Protein Side Chain and Backbone Parameters from ff99SB, J. Chem. Theory Comput. 11 (2015) 3696–3713. doi:10.1021/acs.jctc.5b00255.

[31] S.K. Nayak, K.N. Venugopala, D. Chopra, Vasu, T.N.G. Row, Effect of substitution on molecular conformation and packing features in a series of aryl substituted ethyl-6-methyl-4-phenyl-2-thioxo-1,2,3,4- tetrahydropyrimidine-5-carboxylates, CrystEngComm. 12 (2010) 1205–1216. doi:10.1039/b919648j.

[32] b G.U. and P.V. C. Oliver Kappe,a,* Oleg V. Shishkin, X-ray crystallographic, Tetrahedron. 56 (2000) 1859–1862. doi:10.1016.

[33] A. Dhandapani, S. Manivarman, S. Subashchandrabose, Synthesis, single crystal structure, Hirshfeld surface and theoretical investigations on pyrimidine derivative, Chem. Phys. Lett. 655–656 (2016) 17–29. doi:10.1016/j.cplett.2016.04.009.

[34] S. Chitra, K. Pandiarajan, N. Anuradha, A. Thiruvalluvar, 5-Acetyl-4-(4-methoxyphenyl)-6-methyl-3,4-dihydropyrimidin-2(1H)-one, Acta Crystallogr. Sect. E Struct. Reports Online. 65 (2008). doi:10.1107/S1600536808040270.

[35] Z.-H. Shang, Y. Xiu, Y.-Y. Lin, Ethyl 4-(4-hydroxy-3-methoxyphenyl)-6-methyl-2-thioxo-1,2,3,4-tetrahydropyrimidine-5-carboxylate, Acta Crystallogr. Sect. E Struct. Reports Online. 63 (2007) o4172–o4172. doi:10.1107/S1600536807046752.

[36] G.R. Desiraju, Supramolecular Synthons in Crystal Engineering—A New Organic Synthesis, Angew. Chemie Int. Ed. English. 34 (1995) 2311–2327. doi:10.1002/anie.199523111.

[37] C.L. Heredia, V. Ferraresi-Curotto, M.B. López, Characterization of Ptn (n=2–12) clusters through global reactivity descriptors and vibrational spectroscopy, a theoretical study, Comput. Mater. Sci. 53 (2012) 18–24. doi:10.1016/j.commatsci.2011.09.005.

[38] N.Z. Alzoman, Y.S. Mary, C.Y. Panicker, I.A. Al-Swaidan, A.A. El-Emam, O.A. Al-Deeb, A.A. Al-Saadi, C. Van Alsenoy, J.A. War, Spectroscopic investigation (FT-IR and FT-Raman), vibrational assignments, HOMO–LUMO, NBO, MEP analysis and molecular docking study of 2-[(4-chlorobenzyl)sulfanyl]-4-(2-methylpropyl)-6-(phenylsulfanyl)-pyrimidine-5-carbonitrile, a potential chemotherapeut, Spectrochim. Acta Part A Mol. Biomol. Spectrosc. 139 (2015) 413–424. doi:10.1016/j.saa.2014.12.043.

[39] E. İnkaya, M. Dinçer, E. Şahan, İ. Yıldırım, Synthesis, spectroscopic and structural characterization of 5-benzoyl-4-phenyl-2-methylthio-1H-pyrimidine with theoretical calculations using density functional theory, Spectrochim. Acta Part A Mol. Biomol. Spectrosc. 114 (2013) 92–100. doi:10.1016/j.saa.2013.05.050.

[40] D.L. Pavia, G.M. Lampman, G.S. Kriz, J.A. Vyvyan, Introduction to Spectroscopy, 5th Editio, Cengage Learning, Mason, Ohio, 2015.

[41] AID 485360 - qHTS Assay for the Inhibitors of L3MBTL1 - PubChem, (n.d.). https://pubchem.ncbi.nlm.nih.gov/bioassay/485360#section=Information-Sources (accessed September 12, 2018).

[42] J.M. Herold, T.J. Wigle, J.L. Norris, R. Lam, V.K. Korboukh, C. Gao, L.A. Ingerman, D.B. Kireev, G. Senisterra, M. Vedadi, A. Tripathy, P.J. Brown, C.H. Arrowsmith, J. Jin, W.P. Janzen, S. V. Frye, Small-Molecule Ligands of Methyl-Lysine Binding Proteins, J. Med. Chem. 54 (2011) 2504–2511. doi:10.1021/jm200045v.

[43] N. Gurvich, F. Perna, A. Farina, F. Voza, S. Menendez, J. Hurwitz, S.D. Nimer, L3MBTL1 polycomb protein, a candidate tumor suppressor in del(20q12) myeloid disorders, is essential

for genome stability., Proc. Natl. Acad. Sci. U. S. A. 107 (2010) 22552–7. doi:10.1073/pnas.1017092108.

[44] J. Min, A. Allali-Hassani, N. Nady, C. Qi, H. Ouyang, Y. Liu, F. MacKenzie, M. Vedadi, C.H. Arrowsmith, L3MBTL1 recognition of mono- and dimethylated histones, Nat. Struct. Mol. Biol. 14 (2007) 1229–1231. http://go.galegroup.com/ps/anonymous?id=GALE%7CA185248857&sid=googleScholar&v=2.1&it=r&linkaccess=abs&issn=15459993&p=AONE&sw=w (accessed September 12, 2018).

[45] R.A. Friesner, J.L. Banks, R.B. Murphy, T.A. Halgren, J.J. Klicic, D.T. Mainz, M.P. Repasky, E.H. Knoll, M. Shelley, J.K. Perry, D.E. Shaw, P. Francis, P.S. Shenkin, Glide: A New Approach for Rapid, Accurate Docking and Scoring. 1. Method and Assessment of Docking Accuracy, J. Med. Chem. 47 (2004) 1739–1749. doi:10.1021/jm0306430.

[46] B. Kramer, M. Rarey, T. Lengauer, Evaluation of the FLEXX incremental construction algorithm for protein-ligand docking., Proteins. 37 (1999) 228–41. http://www.ncbi.nlm.nih.gov/pubmed/10584068 (accessed September 12, 2018).

[47] Y. Itoh, T. Suzuki, N. Miyata, Small-molecular modulators of cancer-associated epigenetic mechanisms, Mol. Biosyst. 9 (2013) 873. doi:10.1039/c3mb25410k.

UNIVERSIDADE ESTADUAL DE GOIÁS
Pró Reitoria de Pesquisa e Pós Graduação
Grupo de Química Teórica e Estrutural de Anápolis

November, 30th, 2018

Highlights

A comprehensive structural study of three dihydropyrimidine (DHPM) derivatives was carried out in this work: single crystal X-ray diffraction (SCXRD), Powder diffraction, Raman, Infrared spectroscopy, Density Functional Theory (DFT) calculations and Molecular Docking.

Sincerely yours,

Dr. Hamilton B. Napolitano
Unidade Universitária de Ciências Exatas e Tecnológicas
Universidade Estadual de Goiás